Journal of Geospatial Surveying (2023) 3:1
DOI: http://doi.org/10.4038/jgs.v3i1.46

ORIGINAL ARTICLE

Modelling Urban Heat Island with Landsat Images and LiDAR Datasets

Şengün, E. *a, b, Arefi, H. a, Aksoy, S. c, Taheri, P. d

[a] Hochschule Mainz - University of Applied Sciences, School of Engineering, Department of Geoinformatics and Surveying, Mainz, Germany

[b] Graduate Institute, Geomatics Engineering Program, Istanbul Technical University, Istanbul, Turkey

[c] Department of Geomatics Engineering, Faculty of Civil Engineering, Istanbul Technical University, Istanbul, Turkey

[d] School of Surveying and Geospatial Engineering, College of Engineering, University of Tehran, Tehran, Iran

ARTICLE INFO

Article history:
Received 31 January 2023
Received in revised form 19 March 2023
Accepted 24 March 2023
Available online 6 April 2023

Keywords:
UHI
Landsat
LiDAR
OSM
GEE

ABSTRACT

The environmental problems caused by rapid and uncontrolled urbanization are increasing day by day. When the needs of the growing population are also in question, urbanization problems become unavoidable when considered on a global scale. Since housing is one of the most important population-related needs, there is an increase in urban areas and an expansion of working areas. Therefore, while urban areas are increasing, forested or green areas are shrinking. Decreasing green areas play a very important role in increasing surface temperature. This increase in cities, which are warmer than the surrounding rural areas, is briefly called Urban Heat Island (UHI). Urban Thermal Field Variance Index (UTFVI) was used to calculate the UHI effect. This index, produced from thermal bands, determines the severity of UHI. For this study, attributes were created using Landsat, LiDAR, and Open Street Map data to estimate UHI severity without the aid of thermal bands. Using these features, a random forest machine learning algorithm was trained, and UHI severity maps were estimated. For the city of Sioux Falls, which was selected as the study area, data for the years 2008 and 2020 were used. UHI forecast maps for these years were produced and compared with ground truth maps.

1 Introduction

Today, when unpredictable population growth is added to the problems brought about by rapid and uncontrolled urbanization, it is seen that the problem has reached a global dimension.

As the needs of the population increased, resources began to be consumed rapidly. To provide more resources, forests, and green areas in urban areas have started to be transformed into factory and industrial areas to provide more businesses (Çelik, 2019). In addition, rapid urban development has also increased the number of multi-story and high-density buildings (Wang et al., 2021). The replacement of green areas in urban areas by asphalt and concrete directly affects air quality, climate change, and global warming, and also increases the temperature in cities. In other words, urban areas are warmer than the surrounding rural areas and this is defined as an Urban Heat Island (UHI). This definition was first used by chemist Luke Howard in the 19th century (Li et al., 2011; Oke, 1982; Voogt and Oke, 2003). Monitoring UHI effects is very important in terms of urban planning and sustainability (Şengün et al., 2022).

UHI significantly affects life in cities. For example, Heaviside et al. (2017) conducted a study on the health effects of UHI. In this study, they state that the stress levels of people living in UHIs are higher than those living in rural areas. In addition, it is noted that the elderly and low-income people suffer more from the effects of UHI. The index showing the severity of the UHI effect has been developed as the Urban Thermal Area Variance Index (UTFVI) (Zhang et al., 2006). This extended index provides Land Surface Temperature (LST) calculation using thermal bands. Then it shows the 6 criteria used for evaluation (Çelik, 2019; Şengün et al., 2022). Also, the LST appears to be very strong in summer and weakest in winter (Jin, 2012).

In another study, moderate resolution imaging spectroradiometer (MODIS) LST data, which covers the years 2000-2019, was used. In order to monitor the UHI effect, 5 cities with the highest population density were selected and UHI density was observed during the day. As a

* Corresponding author: E. Şengün, Hochschule Mainz - University of Applied Sciences, School of Engineering, Department of Geoinformatics and Surveying, Mainz, Germany.

E-mail address: sengun16@itu.edu.tr (E. Şengün).

*The previous version of the same article has been replaced with this version where the word 'tapes' has been changed to 'bands'.

result, it was seen that the UHI effect was the most powerful in the most crowded city and the UHI intensity observed during the day was more than at night. If it is intended to be said to be a common result for these five cities, the intensity of the UHI is the same during the day and it varies according to the size of cities at night (Dewan et al., 2021).

Asadi et al. (2020), using an artificial neural network for high spatial resolution black surface temperature, tried to find potential green roofs. They approached this problem as a regression and found 0.786 R^2 and 0.9566 RMSE.

Local authorities have started introducing redevelopment projects to address the problems caused by climate change and global warming. To this end, the project authorities monitored land-surface temperature changes in six major urban redevelopment areas in Lyon, France, from 2000 to 2017. In the Dock and Garibaldi Street areas, for instance, vegetation cover was increased to reduce heat stress and prevent flooding. The construction of Groupama Stadium was in forested and agricultural areas. To monitor changes in vegetation cover, soil moisture content, and built areas, indices such as NDVI (Normalized Difference Vegetation Index), MNDWI (Modified Normalized Difference Water Index), NDMI (Normalized Difference Moisture Index), NDBI (Normalized Difference Built-up Index), and NDBaI (Normalized Difference Bareness Index) were analyzed. The results showed that the Confluence and Kaplan sites experienced an increase in vegetation cover and moisture, resulting in a decrease in surface temperature. In contrast, the Groupama Stadium area experienced an increase in surface temperature and a shrink in vegetation cover. Moreover, the museum, Dock, and Garibaldi sites did not show a monotype trend, but rather an increase in surface temperature in some of the tests. These different results highlight the need to include vegetation in future studies (Renard et al., 2019).

The vegetative layers grown on rooftops are called "green roofs" or "rooftop gardens" and have many advantages. First of all, they seem to reduce the flow of rainwater. They also act as filters for greenhouse gas emissions and pollutants. Moreover, while the majority of summer precipitation is retained by green roofs, only 1/5 of it is retained in winter. The seasonal and precipitation patterns highlight the vital role of green roofs in controlling rainwater and emphasize the importance of implementing them (Vardhu and Sharma, 2023).

Scientists at Lawrence Berkeley National Laboratory have found that while green roof coverings are more expensive than traditional roofs, green roofs have a lifespan of about 50 years and are more advantageous in the long run.

City planners are proposing green roof coverings as a means of reducing the effects of UHI, and suggest that the correlation between various urban characteristics and advanced models must be carefully determined for effective implementation. In this context, Austin, Texas, was chosen as the study area to investigate the effects of the green roof strategy on cooling. The study used Landsat 8 TIRS data from July 2016 to produce LST images, and LIDAR data to create 3D urban morphology models. To simulate the green roof strategy, NDVI and NDBI indexes were calculated from Sentinel 2A satellite images. A multilayer feedforward neural network was then employed to identify the simultaneous relationship between various urban parameters and LST. Selected houses and offices located in the city center were designated for green roof implementation, and the most suitable structures for the application of green roofs were identified to reduce simulation-based urban indicators and LST. The results show that by greening 3.2% of roofs, the average LST decreased by approximately 2°C. The paper summarizes that buildings with green roofs have the largest cooling effect on LST (Asadi et al., 2020).

In addition to the green roof proposal, the use of Green Tree Barrier (GTB) systems in the urban environment has also shown that it reduces air temperature by providing cooling by shading not only on horizontal but also on vertical surfaces (Hayes et al., 2022).

It is generally known that urban materials have darker colors and higher heat capacity compared to vegetation. Areas covered with dark materials tend to absorb and store incoming solar energy. The radiation absorbed by the surface can then be transmitted to the surrounding area through conduction or returned to the urban environment through radiation or convection (Hendel, 2020).

Increasing the total solar reflectance is an economical strategy to reduce heat generation (Maharjan et al., 2020). For this, the use of cold materials such as IR reflective paints and coatings is increasing day by day (Coser et al., 2015). Among the proposed technologies for the optimization of urban structures, it is seen that the preference for cold roofing materials in roof coverings and the use of highly reflective coatings on building surfaces reduce the average temperature in the indoor air. However, the use of highly reflective materials is only suitable for low-rise buildings and roofs, since the solar radiation is largely diffused (Garshasbi et al., 2020; Thejus et al., 2021). Considering today's urban models, it is predicted that high-rise and high-density urbanizations predominate, so materials with high reflectivity will repeatedly reflect solar radiation between buildings and roads. It can be concluded that traditional highly reflective materials do not provide enough advantages, as the capture of solar radiation by urban surfaces will also increase the UHI effect (Morini et al., 2017; Rossi et al., 2016; Wang et al., 2021).

As a solution, the use of retro-reflective materials is recommended instead of traditional high-reflective materials in roof or surface coatings, due to their ability to reflect solar radiation in a very thin layer along the incoming direction (Wang et al., 2021).

2 Study Area and Data Used

In this study, the city of Sioux Falls, located in the US and the most populous city of South Dakota, whose growth is on the rise with the migrations it receives every year, which is very rich in terms of history and socio-cultural terms, was chosen as the study area and is shown in Fig. 1. In this city, just as in other parts of the world, the effects of the places that have changed due to the gains and losses on the land as a trace of human destruction have been examined. It has also been associated with the help of satellite images.

It is located at 43° 32′ 18″ North and 96° 43′ 55″ West. The city is built on an area of approximately 190 km^2. This study has focused on two different years, 2008 and 2020, to compare the same place in order to assess the UHI change (Db-city, 2023).

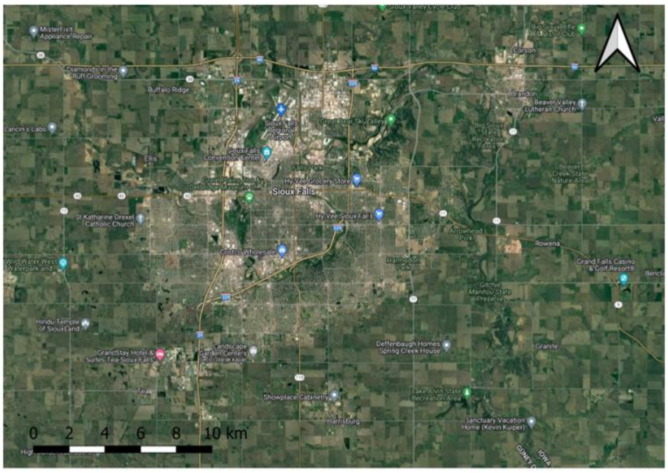

Fig. 1: Study Area (Sioux Falls in the U.S.).

2.1 Landsat Data

The Landsat program is the longest-running earth observation satellite program that is providing earth surface images since 1972. From then, the Landsat program acquires many satellite images throughout the year. Therefore, it has a very wide archive and so is suitable for historical analysis such as change detections. In order to be a base for future studies, first of all, images that are clear in terms of cloudiness and have no radiometric errors were carefully selected from the USGS website. Then, Level 2, Collection 2 data from Landsat collections were used to avoid image preprocessing steps such as atmospheric correction or radiometric correction. Landsat Level-2 products were produced using Collection 2 Level-1 data.

Since Landsat C2 consistently calibrates L1 data and offers the latest developments in data access and data processing, distribution, and algorithm development, using C2, L2 data for studies have been extremely efficient.

Landsat 8 image acquired on 17 September 2020 and Landsat 5 image belonging to the date of 16 September 2008 are used in this study.

2.2 Open Street Map Data

In this study, Open Street Map road data has been utilized. Overpass turbo service is used to obtain the 2020 and 2012 road maps. Since there is no earlier data from 2012 in Open Street Map for this study area, the year 2008 UHI analysis was carried out on this data.

2.3 Traffic Vehicle Counts

There are 617 stations data from 1991 to the present and data for the years 2008 and 2020 have been obtained from Sioux Falls open data program.

2.4 LiDAR Data

Light Detection and Ranging (LiDAR) data are obtained from U.S. Geological Survey 3D Elevation Program (3DEP) for 2008 and 2020. It is providing nationwide 3D point cloud data and elevation data for the U.S.

3 Methodology

The methodology of this study is summarized in Fig. 2. Firstly, Landsat satellite images were found for the derivation of Landsat based features. Using the thermal bands of the Landsat satellites, the UTFVI index was also calculated. Secondly, Open Street Map road data were obtained for two different years. Then, for every pixel in the Landsat images, the nearest road distance was calculated and the grid product was produced. Traffic vehicle count data served as vector point data. To spread out the field, the inverse distance weighting method was established. The final part of the feature derivation is the LiDAR part. LiDAR point clouds are obtained from 3DEP, and points are processed to obtain LiDAR based features. All produced features are combined as predictors for the machine learning algorithm. After model training, accuracy assessments and results maps were produced.

The Digital Terrain Model (DTM) and the Digital Surface Model (DSM) were created with the help of the Point Data Abstraction Library (PDAL) which is developed by (Butler et al. (2023). The Cloth Simulation Filter (CSF) was used for the classification of ground points in the pipeline of DSM. In general, filters appear to perform better on dense data compared to low or medium-density data. One of the filters that perform well on medium-density data is CSF (Štular and Lozić, 2020). The CSF algorithm was preferred because it performs well in areas with high building dominance or on flat terrain (Klápště et al., 2020). The DSM pipeline is similar to DTM except for the ground point classification. All the steps for LiDAR data processing are shown in Fig. 3 which is a modified version described in Bell et al. (2023).

The Landsat OLI/TIRS satellite image used in this study was selected for 2020, and the Landsat 5 TM satellite image for 2008. Level 2 Collection 2 images are used to eliminate preprocessing steps such as geometric or atmospheric correction or orthorectification. It is stated that the above-mentioned sensors produce surface reflection and surface temperature data (Şengün et al., 2022).

Google Earth Engine (GEE) is a cloud-based platform that is capable of processing geospatial data. It is providing both the data and algorithms. GEE offers a multi-petabyte data catalog without the complexity of supercomputers. It is widely used for many applications (Gorelick et al., 2017).

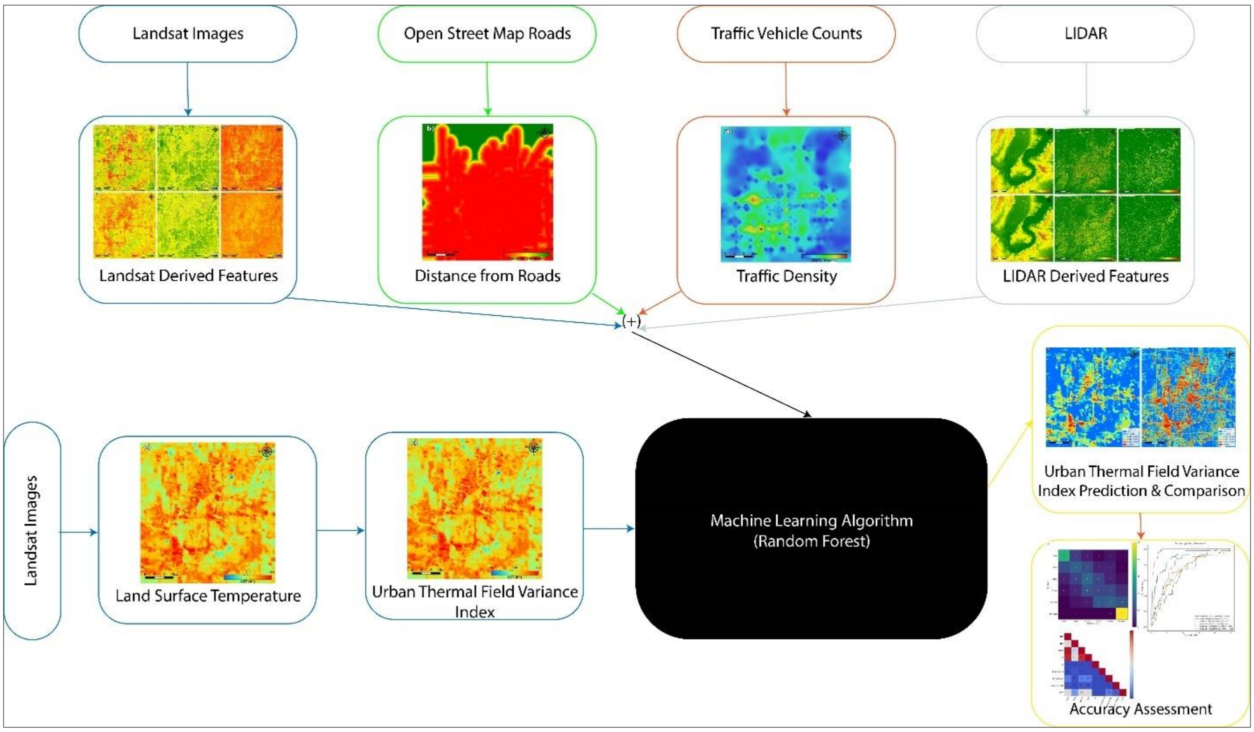

Fig. 2: Flowchart of the methodology.

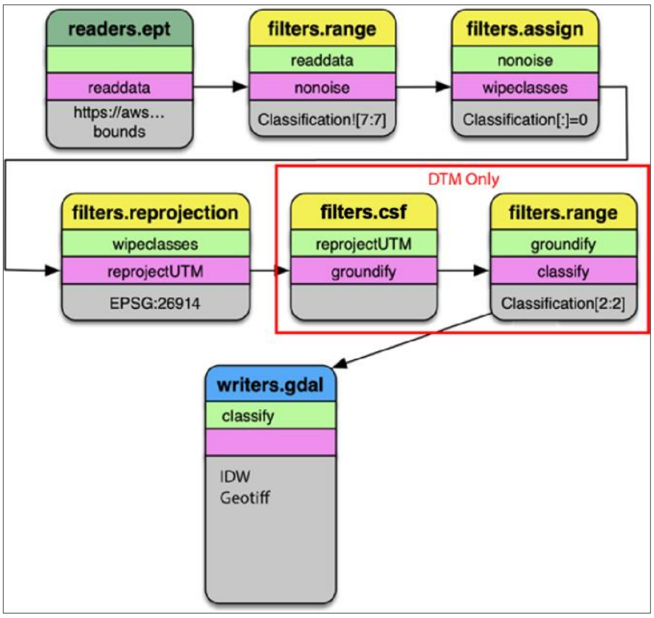

Fig. 3: DSM and DTM deriving pipeline which is used in PDAL (Bell et al., 2023).

The indices calculated using GEE with the help of Landsat satellite images for 2008 and 2020 are the Normalized Difference Vegetation Index (NDVI), the Normalized Difference Built-up Index (NDBI), Index-based Built-up Index (IBI), The Modified Normalized Difference Water Index (MNDWI), Soil Adjusted Vegetation Index (SAVI).

Features calculated using LiDAR data are also: DSM, DTM, normalized Digital Surface Model (nDSM), and Building Volume (BV). DSM is derived from all LiDAR points as described in Fig. 3. DTM is the version of a DSM map that is produced by using only the ground points. The points are classified as building and ground points in the pipeline as shown in Fig. 4. After that, nDSM is derived from the difference between DSM and DTM. nDSM is showing building height because of the building points classified during the DTM deriving process. The Building Volume (BV) was ultimately ascertained by the multiplication of the building height (nDSM) by the area of the building, represented as a grid map, for each corresponding pixel of a 1 ha expanse as elucidated in Table 1.

Necessary maps of the study area were downloaded from Open Street Map and distance maps were produced. Each pixel contained the closest path. As a result, the traffic maps created from the point traffic density data were created in GEE and the Inverse Distance Weighting (IDW) method was used. A traffic density map was produced for the prediction of UHI. The number of vehicles here shows the total number of vehicles passing through the station in 1 year.

NDVI is a vegetation measurement index that scientists frequently use in remote sensing. It is calculated using the NIR and Red channels, as seen in equation 1. The NDVI range ranges from -1 to +1 and healthy plant values are close to +1 (Rouse et al., 1973). In this study, the NIR band of Landsat 5 (0.76-0.90 wavelength range) and Landsat 8 (0.85-0.88 wavelength range) were used.

$$(NIR - Red)/(NIR + Red) \quad (1)$$

The SAVI index is an indicator utilized to mitigate the influence of soil brightness. Their values range from -1 to +1. As seen in equation 2, NIR band pixel values, red band pixel values, and the amount of green vegetation cover are used in its calculation (Huete, 1988). In this study, the NIR band of Landsat 5 (0.76-0.90 wavelength range) and Landsat 8 (0.85-0.88 wavelength range) were used.

$$(NIR - RED)/(NIR + RED + L)) * (1 + L) \quad (2)$$

L: Amount of green vegetation cover

The Normalized Difference Water Index (NDWI) was overestimated by the extracted water area because the water information obtained was often confused with on-board terrain noise. The modified NDWI (MNDWI) is more suitable for developing water information as it offers advantages such as reducing or even eliminating on-board land noise. The formula is shown in equation 3. In this study, the Shortwave Infrared (SWIR) band of Landsat 5 (2.08-2.35 wavelength range) and Landsat 8 (1.57-1.65 wavelength range) were used.

$$(GREEN - SWIR) / (GREEN + SWIR) \quad (3)$$

The index used to show urban and residential areas is NDBI. It is an important index used to understand the changes in land cover that occur in cities and their surroundings. As seen in equation 4, SWIR and NIR bands were used (Zha et al., 2003). In this study, the SWIR band of Landsat 5 (2.08-2.35 wavelength range) and Landsat 8 (1.57-1.65 wavelength range), and the NIR band of Landsat 5 (0.76-0.90 wavelength range) and Landsat 8 (0.85-0.88 wavelength range) were used.

$$(SWIR1 - NIR)/(SWIR1 + NIR) \quad (4)$$

This index is a new index created to describe built-up land features. In this respect, it offers a very innovative approach and uses the NDBI, SAVI, and MNDWI indices as seen in equation 5 (Xu, 2008).

$$[NDBI - (SAVI + MNDWI)/ 2]/[NDBI + (SAVI + MNDWI)/2] \quad (5)$$

In order to perceive the effect of urban structures in city centers on UHI, 3D urban morphology models need to be created. This process is done by extracting DTM data representing building heights from the digital surface model DSM. It is shown in the formula below.

$$nDSM = DSM - DTM \quad (6)$$

It is an expression that shows the amount of building density in a unit cell (Asadi et al., 2020).

$$nDSM * Height \quad (7)$$

It is very important to use the UTFVI index for the quantitative analysis of the UHI effect. As shown in equation 8, it is the value found by subtracting the LSTm value representing the average ground surface temperature from the LST and dividing the result obtained by the ground surface temperature again (Renard et al., 2019).

$$UTFVI = \frac{LST - LST_m}{LST} \quad (8)$$

To model this phenomenon using these features, the random forest algorithm has been utilized.

The random forest algorithm is developed by Breiman (2001). It uses classification and regression trees (CART) as ensemble learning to overcome weak learners' problems which CART has. It can achieve strong learning by using parallel uncorrelated CART. It can be used for both classification and regression (Breiman, 2001).

The 6 criteria of the UTFVI index used to highlight the city areas affected by UHI can be briefly shown in Table 1 with their corresponding ecological evaluations (Renard et al., 2019).

Table 1: Ecological assessment criteria of UTFVI (Renard et al., 2019).

UTFVI	UHI phenomenon	Ecological evaluation
< 0	None	Excellent
0.000 – 0.005	Weak	Good
0.005 – 0.010	Middle	Normal
0.010 – 0.015	Strong	Bad
0.015 – 0.020	Stronger	Worse
> 0.020	Strongest	Worst

To train the model, 200 stratified points were selected for each UHI phenomenon class described in Table 1. Six totally different classes were investigated as UHI phenomenon severities. The purpose of using the dots is to sample the feature values in the images described earlier. For this, the RF algorithm in GEE is used. Then, using the created feature maps, the UTFVI maps were predicted with this model.

4 Results and Discussion

UHI phenomenon severity maps are produced using LST maps. LST maps have 120 m spatial resolution due to Landsat thermal band spatial resolution. These maps are used as ground truth for the prediction of the UTFVI maps.

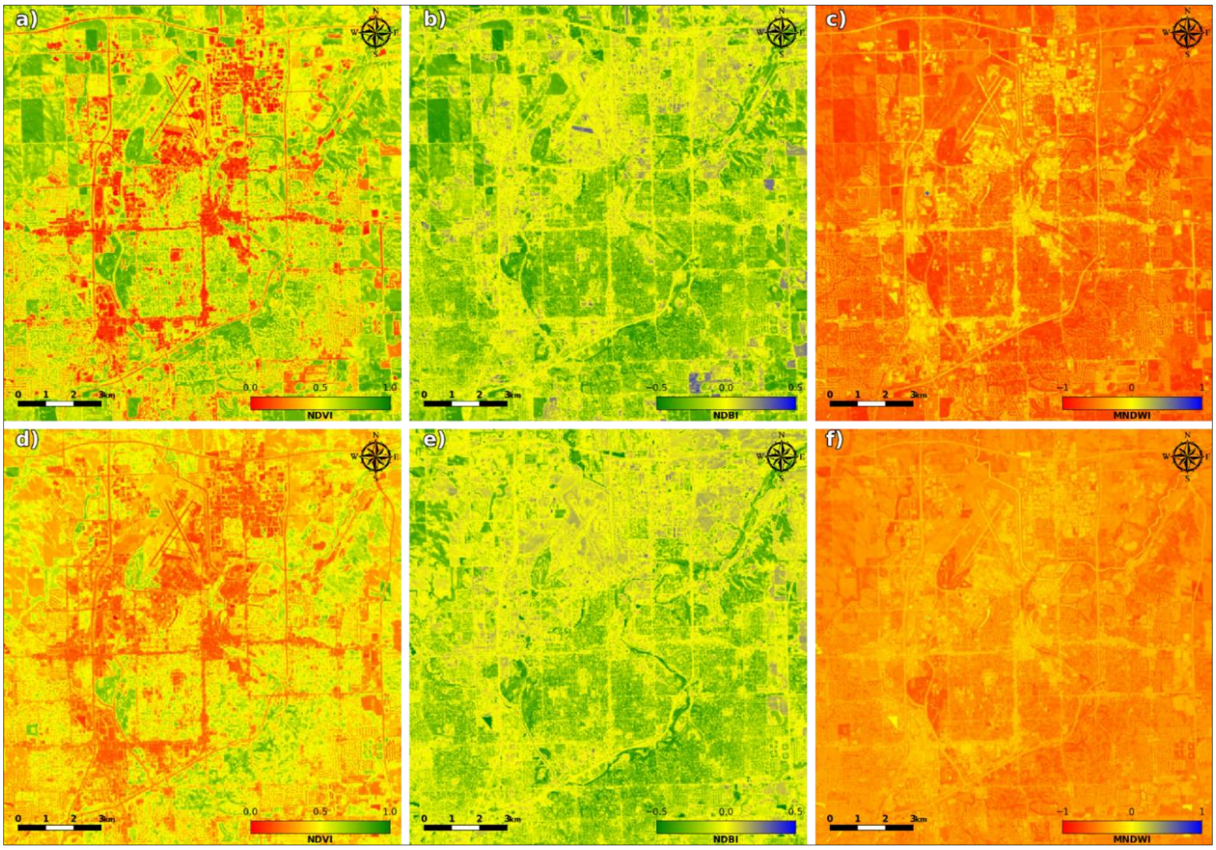

Fig. 4: Feature maps: a) 2008 NDVI, b) 2008 NDBI, c) 2008 MNDWI, d) 2020 NDVI, e) 2020 NDBI, and f) 2020 MNDWI.

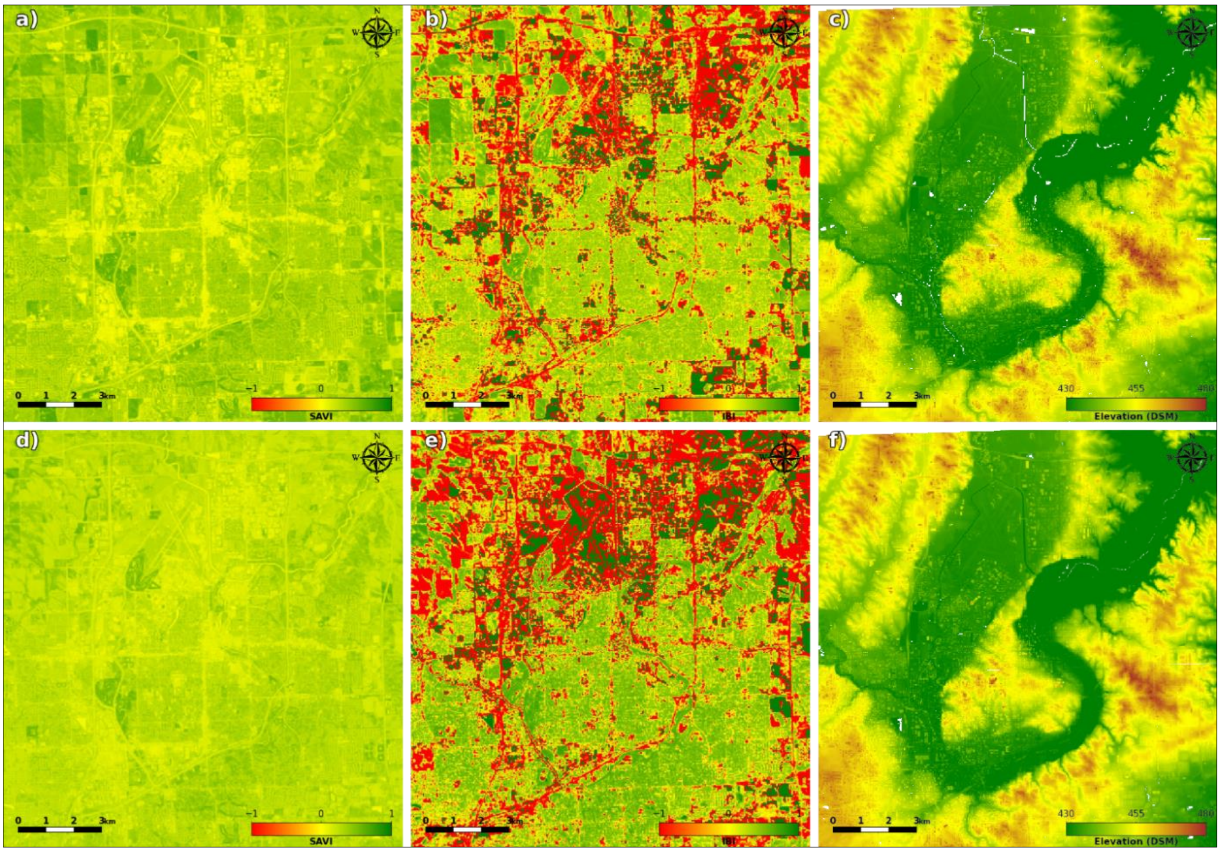

Fig. 5: Feature maps: a) 2008 SAVI, b) 2008 IBI, c) 2008 DSM, d) 2020 SAVI, e) 2020 IBI, and f) 2020 DSM.

To develop a model that predicts UTFVI maps, the features mentioned in the methodology section are generated. Fig. 4 shows the feature maps which are derived from Landsat 5 and 8 satellite images.

In addition to Landsat derived features, LiDAR derived features are also produced. They have been shown in Fig. 5. In Fig. 5, along with the SAVI and IBI indices, DSM is also shown. City elevation is changing from 430 m to 480 m respectively. When the IBI map is investigated, it is clear that the city has expanded through the years.

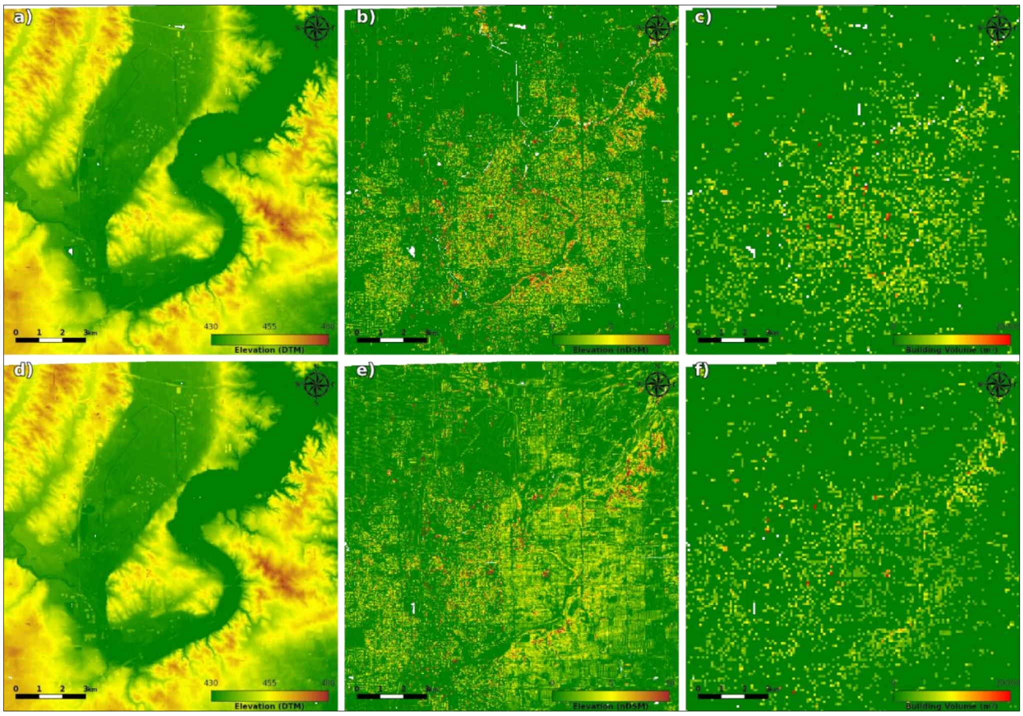

Fig. 6: Feature maps: a) 2008 DTM, b) 2008 nDSM, c) 2008 Building Volume, d) 2020 DTM, e) 2020 nDSM, and f) 2020 Building Volume.

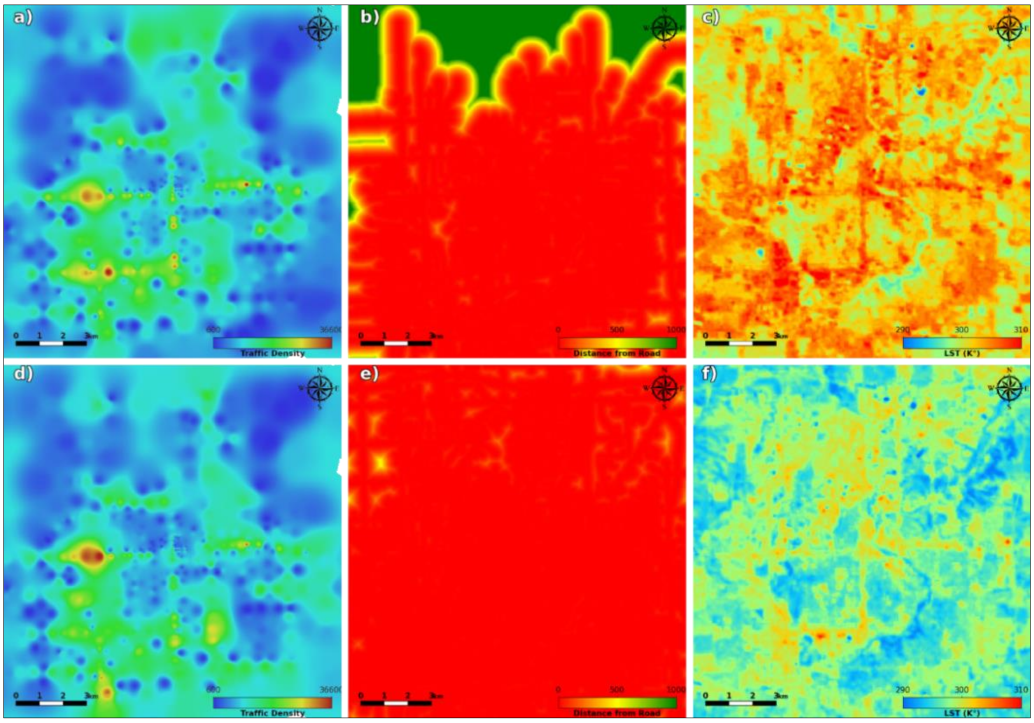

Fig. 7: Feature maps a) 2008 Traffic Density, b) 2008 Distance from Road, c) 2008 LST, d) 2020 Traffic Density, e) 2020 Distance from Road, and f) 2020 LST.

Only LiDAR derived feature maps are shown in Fig. 6. When Fig. 6 is investigated, it is obvious that DSM and DTM are very similar to each other. However, an object such as a building has been removed in DTM and can be seen clearly. The difference between DSM and DTM has shown as nDSM as described in the methodology. Building height can easily be seen by it. Moreover, more buildings are present in the 2020 maps, and taller buildings are also frequent.

The last feature map partition is shown in Fig. 7. Traffic density is produced by the inverse distance weighting method, distance from roads, and land surface temperature map. When Fig. 7 is investigated, it is obvious that some of the areas in the city are warmer than the rural areas. Furthermore, LST maps show the year 2008 is warmer than 2020 on that specific date. On another point, traffic has increased in specific regions between the two years.

Correlation heat maps are very useful to see correlations between features. To this end correlation heat maps were produced for each year. They have been shown in Fig. 8 and Fig. 9 and they are also very similar to each other, especially the UTFVI correlations.

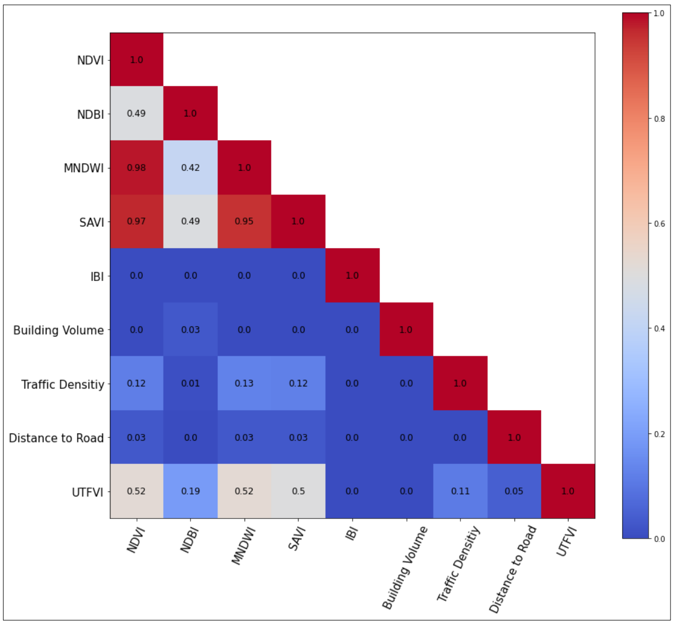

Fig. 8: Correlation heat maps of the feature maps in the year 2008.

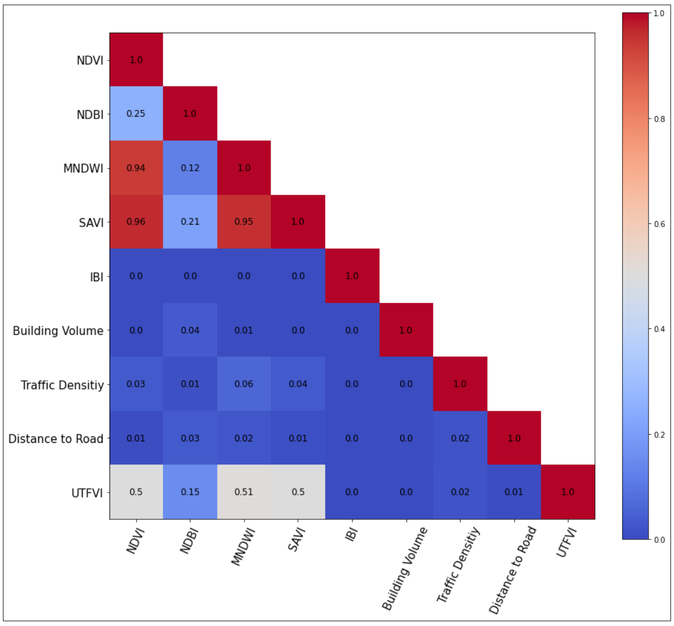

Fig. 9: Correlation heat maps of the feature maps in the year 2020.

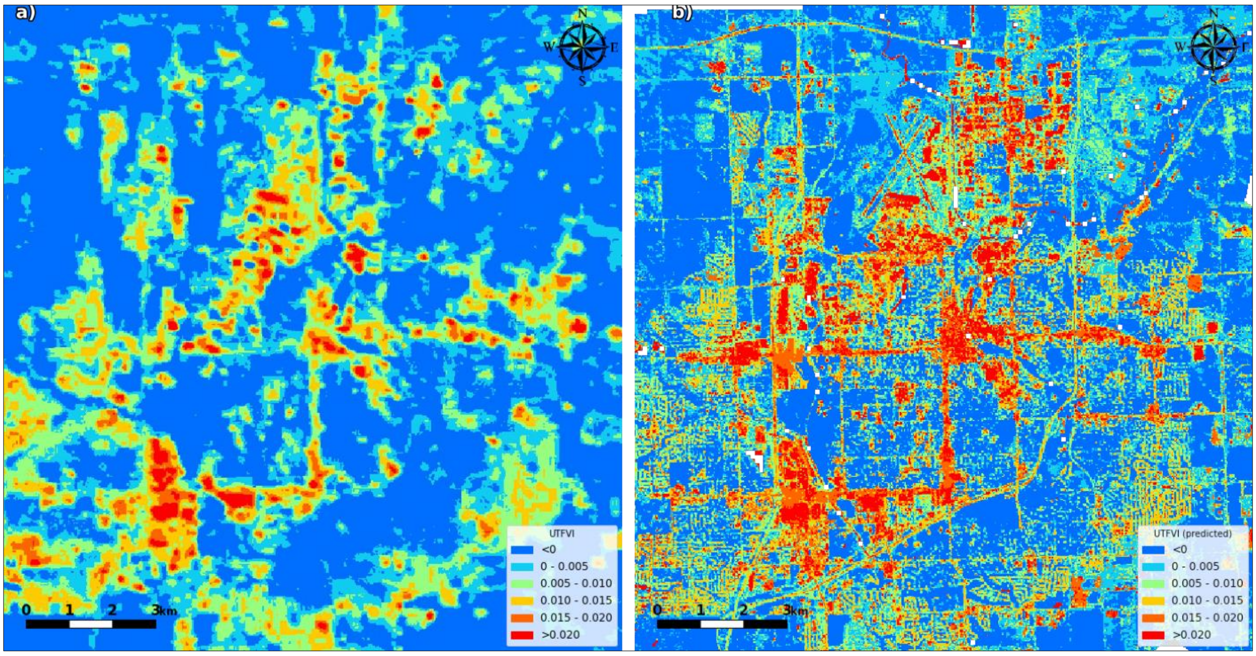

Fig. 10: UHI severity maps: a) 2008 Ground Truth Map, b) 2008 Predicted Map.

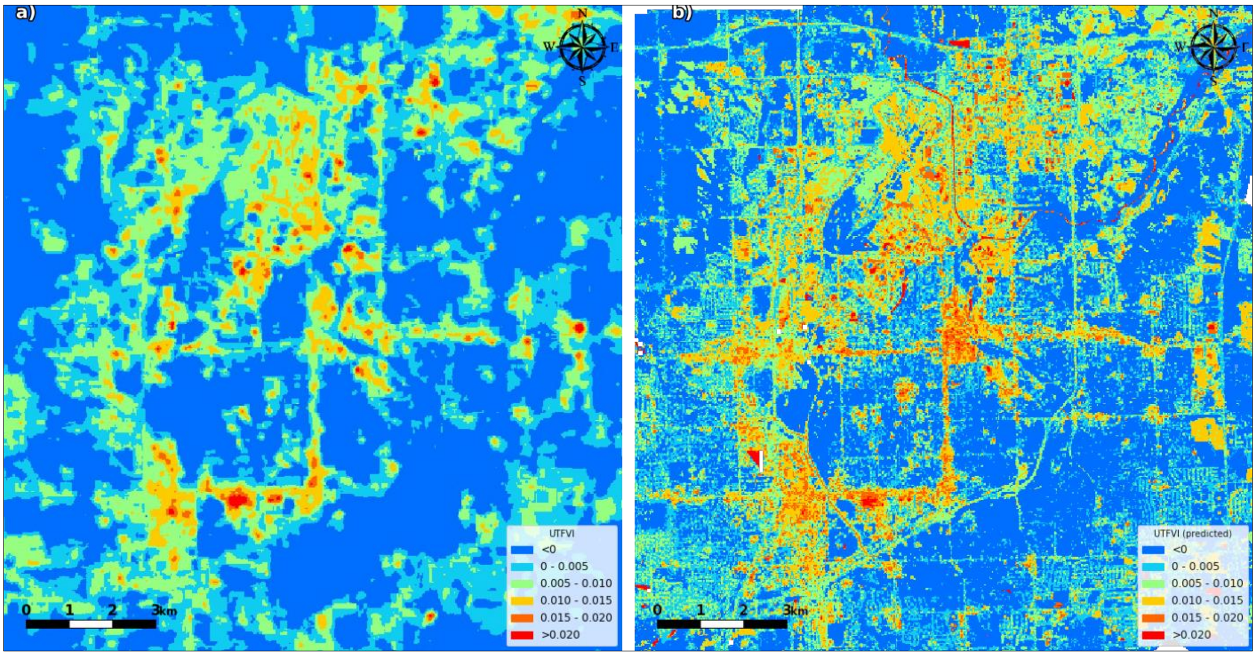

Fig. 11: UHI severity: maps a) 2020 Ground Truth Map, b) 2020 Predicted Map.

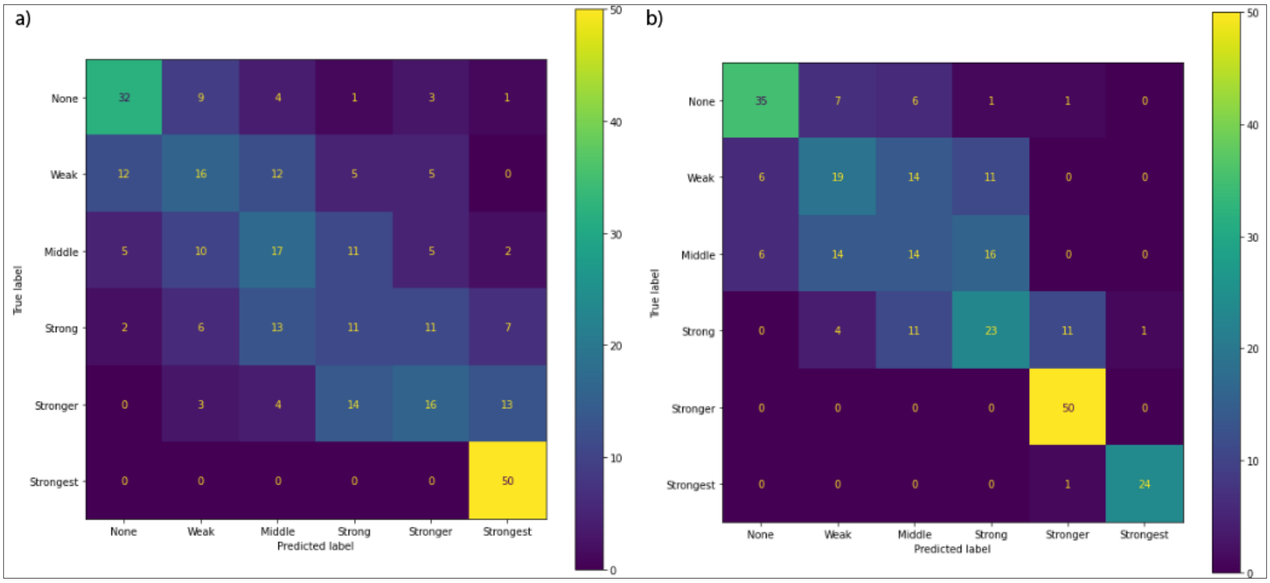

Fig. 12: Confusion matrix of accuracy assessment for a) 2008 b) 2020.

A comparison of the produced ground truth maps with the predicted UTFVI maps by years is shown in Fig. 10 and Fig. 11. Considering the 6 ecological evaluation criteria of the UTFVI index, especially the places shown in red, show the places with heavy traffic and the places where the building density is high. Accordingly, the places with a lot of red colors on the map represent the places where the UHI intensity is high. Especially the red color intensity at the junction points emphasizes the UHI intensity. In blue color, it is stated that the UHI severity is zero, that is, ineffective. The places between these two colors are under the influence of warmer UHI. The primary aim of this study is the assessment of the severity of UHI without using thermal band-aids. In addition to that, due to the spatial resolution of the features that have been used to model UHI, predicted UTFVI maps have 30 m spatial resolution and which is higher than the ground truth maps. When maps are interpreted visually, roads and nearing facilities that have higher severity of UHI can be seen more clearly in the prediction maps because of the higher spatial resolution of the features. However, for the year 2008 prediction map, UHI severity was overestimated when compared to the ground truth map. When the year 2008 and the year 2020 UHI severity maps are compared, the year 2008 map has much higher severities. The reason for that is the year 2008 is much warmer than the year 2020. UHI severities will increase with the temperature. Prediction maps show much more spatial detail when compared to the UTFVI maps which are derived from the thermal band.

In order to evaluate the accuracy, 50 stratified points were selected for each class, different from those in the training set. These selected points were used to sample the predicted map and ground truth map UTFVI classes for accuracy assessment.

Using these examples, error matrices were created for both years and shown in Fig. 12. When the error matrices are checked, the accuracy evaluation for 2008 is 0.45; it is seen that the accuracy assessment for 2020 is 0.64. It is thought that the reason for the low evaluation of 2008 is the use of road data from 2012 since there is no road data for 2008.

The accuracy of the model was also investigated using a variation curve of points also known as the receiver operating characteristic. We have employed 6 classes of UHI ecological evaluation. For 2008 and 2020 these graphs are shown in Fig. 13 and Fig. 14. They have both shown Stronger and None affected areas have a more accurate model. Middle and Near Severities are hard to distinguish each other so the Area Under Curve values are lower.

When this study's results are compared to a similar study by Asadi et al. (2020), this study differs in the methodological perspective. They employed an artificial neural network to model the land surface temperature. However, in this study, the ecological evaluation of the urban heat island is modeled. In terms of R^2, they have managed to get 0.775. They also used similar features as this study to develop a model.

Vergara et al. (2023) applied a random forest machine learning regression algorithm to predict the UTFVI index. They achieved an accuracy value of 0.89 R^2. They have used NDVI and NDBI indices as predictors in their study also.

5 Conclusions and Recommendations

UHI was created without a thermal band-aid using satellite images and other data sets of the study area, Sioux Falls. The UHI domain has been interpreted by generating UTFVI ground reality maps and UTFVI predictive maps. The most striking of these comments is that the UHI effect increases dramatically in crowded areas of the city, while it is relatively less in green areas. The lesson that can be drawn from this result, which is valid for both years, is that the green areas should be increased by the relevant institutions of the municipality.

Especially in metropolitan cities, it is possible to make climate-sensitive models if UHI maps are used as a data source to help the preparation process of city plans. Thus, employment is provided with urban land plans made with minimum damage to nature and the rural ecosystem.

This study is performing a machine learning algorithm to determine the UHI effect on a city without the need for thermal imagery. However, finding available LIDAR, traffic density and Open Street Map data is difficult. Moreover, scaling this study to other study areas is hard to accomplish because of that. Furthermore, this study only applies urban heat island prediction from satellite images. On-site data such as meteorological stations can improve the results. Also, the human perspective for UHIs is not considered in this study. Cities are a combination of people and infrastructures. Therefore, UHI has a high impact on humans.

For further studies, much more features can be considered to model this phenomenon. Other machine learning approaches such as support vector machine, XGBoost, or deep learning methods can be utilized.

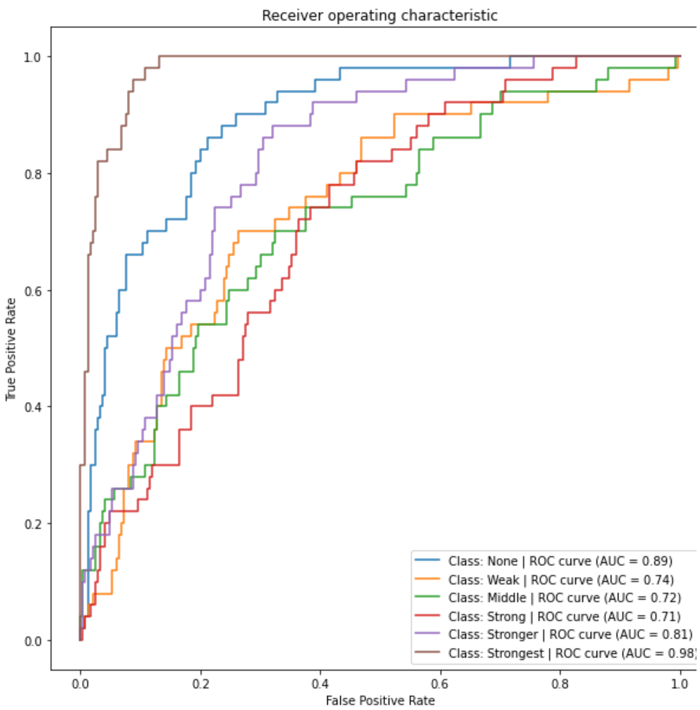

Fig. 13: Receiving operation characteristics for the model that belongs to the year 2008.

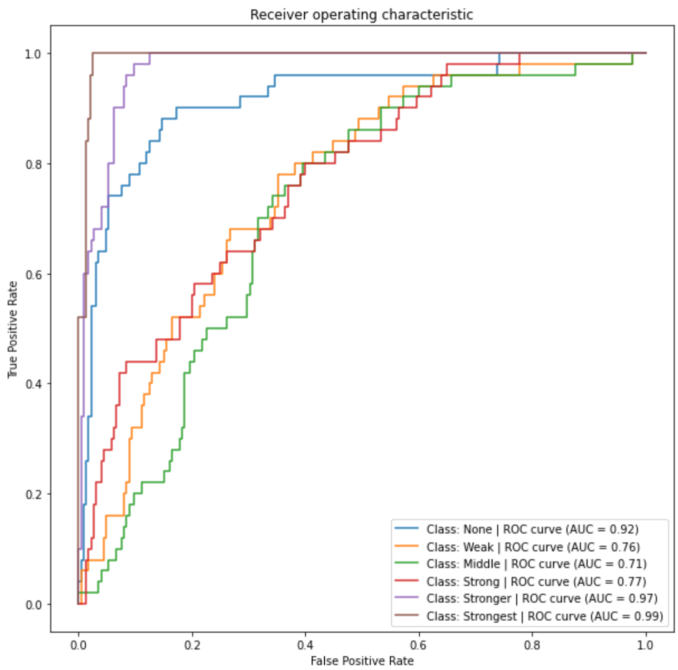

Fig. 14: Receiving operation characteristics for the model that belongs to the year 2020.

Acknowledgment

This research did not receive any specific grant from funding agencies in the public, commercial, or not-for-profit sectors.

Author Contributions

Conceptualization H.A, E.Ş, P.H, methodology and analysis E.Ş., S.A., original draft preparation E.Ş, S.A and writing - review, editing, E.Ş, S.A. All authors have read and agreed to the published version of the manuscript.

Conflict of Interest

The authors declare no conflict of interest.

References

Asadi, A., Arefi, H., Fathipoor, H., 2020. Simulation of green roofs and their potential mitigating effects on the urban heat island using an artificial neural network: A case study in Austin, Texas. Advances in Space Research, 66(8): 1846-1862. DOI:https://doi.org/10.1016/j.asr.2020.06.039

Bell, A., Chambers, B., Butler, H., 2023. Reading data from EPT — pdal.io [WWW Document]. URL https://pdal.io/en/latest/tutorial/iowa-entwine.html (Accessed: 28 February 2023).

Breiman, L., 2001. Random forests. Machine learning, 45: 5-32. DOI:https://doi.org/10.1023/A:1010933404324

Butler, H., Bell, A., Gerlek, M. P., chambbj, Gadomski, P., Manning, C., Łoskot, M., Couwenberg, B., Ramsey, P., Barker, N., Chaulet, N., c42f, Rouault, E., Rosen, M., Lewis, S., Villemin, G., Grigory, McKelvey, K., Mann, K., Brookes, D., Evers, K., Vergara, V., xantares, Yonas, A., Dobias, M., Petras, V., Smith, M. D., Visser, M., Moore, O., 2023. PDAL/PDAL: 2.5.0 (2.5.0). Zenodo.

Çelik, B., 2019. Arazi örtüsü değişimlerinin kentsel ısı adalarına olan etkilerinin zamansal ve mekansal olarak araştırılması (A temporal and spatial investigation of the effects of land cover changes on urban heat islands). Thesis, Istanbul Technical University (ITU). DOI:https://polen.itu.edu.tr/items/0fc2bc8d-94fe-48fe-9223-c648585e1107/full

Coser, E., Moritz, V. F., Krenzinger, A., Ferreira, C. A., 2015. Development of paints with infrared radiation reflective properties. Polímeros, 25: 305-310. DOI:https://doi.org/10.1590/0104-1428.1869

Db-city, 2023. Sioux Falls [WWW Document]. URL https://tr.db-city.com/tr.db-city.com/Amerika-Birle%C5%9Fik-Devletleri--G%C3%BCney-Dakota--Minnehaha--Sioux-Falls (Accessed: 27 January 2023).

Dewan, A., Kiselev, G., Botje, D., 2021. Diurnal and seasonal trends and associated determinants of surface urban heat islands in large Bangladesh cities. Applied Geography, 135. DOI:https://doi.org/10.1016/j.apgeog.2021.102533

Garshasbi, S., Huang, S., Valenta, J., Santamouris, M., 2020. On the combination of quantum dots with near-infrared reflective base coats to maximize their urban overheating mitigation potential. Solar Energy, 211: 111-116.

Gorelick, N., Hancher, M., Dixon, M., Ilyushchenko, S., Thau, D., Moore, R., 2017. Google Earth Engine: Planetary-scale geospatial analysis for everyone. Remote sensing of Environment, 202: 18-27. DOI:https://doi.org/10.1016/j.rse.2017.06.031

Hayes, A. T., Jandaghian, Z., Lacasse, M. A., Gaur, A., Lu, H., Laouadi, A., Ge, H., Wang, L., 2022. Nature-Based Solutions (NBSs) to Mitigate Urban Heat Island (UHI) Effects in Canadian Cities. Buildings, 12(7): 925. DOI:https://doi.org/10.3390/buildings12070925

Heaviside, C., Macintyre, H., Vardoulakis, S., 2017. The urban heat island: implications for health in a changing environment. Current environmental health reports, 4: 296-305. DOI:https://doi.org/10.1007/s40572-017-0150-3

Hendel, M., 2020. 6 - Cool pavements. In: F. Pacheco-Torgal, S. Amirkhanian, H. Wang, E. Schlangen, (Ed.), Eco-Efficient Pavement Construction Materials. Woodhead Publishing Series in Civil and Structural Engineering, Woodhead Publishing, pp. 97–125. https://doi.org/10.1016/B978-0-12-818981-8.00006-0.

Huete, A. R., 1988. A soil-adjusted vegetation index (SAVI). Remote sensing of environment, 25(3): 295-309. DOI:https://doi.org/10.1016/0034-4257(88)90106-X

Jin, M. S., 2012. Developing an index to measure urban heat island effect using satellite land skin temperature and land cover observations. Journal of Climate, 25(18): 6193-6201. DOI:https://doi.org/10.1175/JCLI-D-11-00509.1

Klápště, P., Fogl, M., Barták, V., Gdulová, K., Urban, R., Moudrý, V., 2020. Sensitivity analysis of parameters and contrasting performance of ground filtering algorithms with UAV photogrammetry-based and LiDAR point clouds. International Journal of Digital Earth, 13(12): 1672-1694. DOI:https://doi.org/10.1080/17538947.2020.1791267

Li, J., Song, C., Cao, L., Zhu, F., Meng, X., Wu, J., 2011. Impacts of landscape structure on surface urban heat islands: A case study of Shanghai, China. Remote sensing of environment, 115(12): 3249-3263.

Maharjan, S., Liao, K.-S., Wang, A. J., Curran, S. A., 2020. Highly effective hydrophobic solar reflective coating for building materials: Increasing total solar reflectance via functionalized anatase immobilization in an organosiloxane matrix.

Construction and Building Materials, 243: 118189. DOI:https://doi.org/10.1016/j.conbuildmat.2020.118189

Morini, E., Castellani, B., Presciutti, A., Filipponi, M., Nicolini, A., Rossi, F., 2017. Optic-energy performance improvement of exterior paints for buildings. Energy and Buildings, 139: 690-701. DOI:https://doi.org/10.1016/j.enbuild.2017.01.060

Oke, T. R., 1982. The energetic basis of the urban heat island. Quarterly Journal of the Royal Meteorological Society, 108(455): 1-24. DOI:https://doi.org/10.1002/qj.49710845502

Renard, F., Alonso, L., Fitts, Y., Hadjiosif, A., Comby, J., 2019. Evaluation of the effect of urban redevelopment on surface urban heat islands. Remote Sensing, 11(3): 299. DOI:https://doi.org/10.3390/rs11030299

Rossi, F., Castellani, B., Presciutti, A., Morini, E., Anderini, E., Filipponi, M., Nicolini, A., 2016. Experimental evaluation of urban heat island mitigation potential of retro-reflective pavement in urban canyons. Energy and Buildings, 126: 340-352. DOI:https://doi.org/10.1016/j.enbuild.2016.05.036

Rouse, J. W., Haas, R. H., Schell, J. A., Deering, D. W., 1973. Monitoring vegetation systems in the great plains with ERTS. Proceedings of the Third ERTS-1 Symposium, NASA, Washington D.C., pp. 309–317.

Şengün, E., Alganci, U., Aksoy, S., 2022. Long Term Monitoring of Land Use – Land Cover Change and its Effect on Surface Temperature by Use of LANDSAT Images and Google Earth Engine Platform. GIS Ostrava 2022 Earth Observation for Smart City and Smart Region. DOI:https://doi.org/10.31490/9788024846026-8.

Štular, B., Lozić, E., 2020. Comparison of filters for archaeology-specific ground extraction from airborne LiDAR point clouds. Remote Sensing, 12(18): 3025. DOI:https://doi.org/10.3390/rs12183025

Thejus, P., Krishnapriya, K., Nishanth, K., 2021. A cost-effective intense blue colour inorganic pigment for multifunctional cool roof and anticorrosive coatings. Solar Energy Materials and Solar Cells, 219: 110778. DOI:https://doi.org/10.1016/j.solmat.2020.110778

Vardhu, V. A. K., Sharma, A., 2023. Classification, Mitigations and Methods to Detect UHI: A Review. International Journal of Scientific Research in Engineering and Management (IJSREM), 7(2).

Vergara, D., Blanco, A., Marciano Jr, J., Meneses III, S., Borlongan, N., Sabuito, A., 2023. Assessing and Modelling Urban Heat Island in Baguio City Using Landsat Imagery and Machine Learning. The International Archives of the Photogrammetry, Remote Sensing and Spatial Information Sciences, 48: 457-464. DOI:https://doi.org/10.5194/isprs-archives-XLVIII-4-W6-2022-457-2023

Voogt, J. A., Oke, T. R., 2003. Thermal remote sensing of urban climates. Remote sensing of environment, 86(3): 370-384. DOI:https://doi.org/10.1016/S0034-4257(03)00079-8

Wang, J., Liu, S., Meng, X., Gao, W., Yuan, J., 2021. Application of retro-reflective materials in urban buildings: a comprehensive review. Energy and Buildings, 247: 111137. DOI:https://doi.org/10.1016/j.enbuild.2021.111137

Xu, H., 2008. A new index for delineating built-up land features in satellite imagery. International journal of remote sensing, 29(14): 4269-4276. DOI:https://doi.org/10.1080/01431160802039957

Zha, Y., Gao, J., Ni, S., 2003. Use of normalized difference built-up index in automatically mapping urban areas from TM imagery. International Journal of Remote Sensing, 24(3): 583-594. DOI:https://doi.org/10.1080/01431160304987

Zhang, Y., Yu, T., Gu, X., Zhang, Y.-x., Chen, L.-f., 2006. Land surface temperature retrieval from CBERS-02 IRMSS thermal infrared data and its applications in quantitative analysis of urban heat island effect. Journal of Remote Sensing, 10(5): 789.